Supplementary Document

1T-Phase Titanium Disulfide Nanosheets for Sensing H_2S and O_2

*Neha Sakhuja[+], Ravindra Kumar Jha[+‡], Rajneesh Chaurasiya[#‡], Ambesh Dixit[#] and Navakanta Bhat[+]**

**Email : navakant@iisc.ac.in*

Supplementary Note 1 – UV-VIS Spectroscopy

To understand the optical absorptions of these nanosheets, UV-VIS spectroscopy was performed for all the specimens. The UV VIS absorbance spectra in Figure S3 exhibits broad peak (around 610nm) in visible spectra which is attributed to inter band transitions from near the Fermi level [1]. The blue shift (decrease in wavelength) in position of this major peak along with increase in intensity with the decrease in nanosheets dimensions has been reported in literature [1]. Hence, it is evident that there is increase in intensity as well as blue shift in peak position from bulk (677 nm) to exfoliated (610 nm) TiS_2.

Supplementary Note 2 – Sensor response to 2TNS and 4TNS

The transient sensing response for 2TNS and 4TNS towards H_2S at room temperature is shown in figure S9. The specimen 2TNS shows maximum response of 56.4% towards 4 ppm of H_2S and can resolve till 1 ppm. The other specimen 4TNS shows maximum response of 65.27% towards 4 ppm of H_2S and can detect up to 500 ppb of H_2S. However, the optimized specimen

named 6TNS as discussed in main paper shows the optimal performance with resolution of 300 ppb at room temperature.

Supplementary Note 3 – Sensor fabrication

The sensor was fabricated on a chemically cleaned p-type Silicon substrate which was thermally oxidized to form an electrically insulating layer of 1 μm SiO_2. Subsequently, patterning of Inter-digitated electrodes (IDE's) was carried out on the Si/SiO_2 substrate using optical lithography. The separation as well as the width of the electrodes was fixed to 5μm. Lastly, a thin (10/90 nm) film of Titanium/ Platinum (Ti/Pt) was sputter deposited on the patterned substrate to create contact pads, followed by lift off. The sensing material was drop casted on this fabricated Ti/Pt IDE, which act as a transducer. The SEM image of IDE with and without receptor is shown in Figure S27 respectively.

The van der pauw structure (figure S26) was fabricated to determine the resistivity, hall voltage and carrier concentration of our sample. The dispersed nanosheets were drop casted on a blanket silicon substrate to form a continuous film of approx. a micron thick. The contact pads were made at the four corners of the substrate using Silver paste.

Supplementary Note 4 – Gas Concentration calibration

The gas flow rate (sccm) corresponding to particular concentrations of H_2S and O_2 has been calibrated as follows. Let us consider C_{max} as the maximum concentration of cylinder and C_r as the desired concentration of the analyte under test. Let us assume that the flow rate of reference gas and target gas is denoted by FR_a and FR_g respectively and these flow rates are controlled by Alicat MFC's. Hence C_r can be calculated as follows:

$$C_r = \frac{FR_g}{FR_g + FR_a}\ x\ C_{max.} \quad (1)$$

where, FR_g + FR_a is fixed to 500 sccm.

Using these equations, the desired gas concentration reaching the sensor was determined. The calculated flow rates for target gas and reference gas corresponding to a particular concentration was introduced into the chamber after precisely mixing it using a static mixture. The flow rate values corresponding to different concentrations of H_2S and O_2 has been tabulated as follows:

Table S1 : Flow rates corresponding to H_2S concentrations introduced into the chamber

Concentration (ppm)	Reference gas (sccm)-Dry air	Target gas (sccm) – H_2S
0.3	26.79	473.21
0.5	44.64	455.36
1	89.29	410.71
3	232.14	267.86
4	357.14	142.86

Table S2 : Flow rates corresponding to O_2 concentrations introduced into the chamber

Concentration (in %)	Reference gas (sccm)-N_2	Target gas (sccm) – O_2
1	495	5
5	495	25
15	425	75
25	375	125
50	250	250
75	125	375
100	0	500

Supplementary Note 5 – Mechanism of Liquid Exfoliation

Liquid exfoliation works on the principle of acoustic cavitation[2]. The layered material is exposed to intense ultrasonic waves in a solvent. Due to ultrasonic waves, high vapor pressure is achieved leading to high-intensity cavitation bubble. These bubbles grow in negative pressure zone while shrink in positive pressure zone of acoustic field. Hence, the continuous interaction of bubbles and acoustic field results into growth and ultimate collapse of these cavitation bubbles. Subsequently high-energy jets are created on the surface of bulk material, breaking up the bulk crystallite into exfoliated nanosheets. Hence, the resulting hydrodynamic forces aid in disintegration of agglomerates dissolved in solvent. The choice of solvent is another determining factor in liquid exfoliation. If the surface tension of solvent is mismatched with that of the 2D material, the balance of stabilization and reaggregation is broken due to the continuous Brownian motion of solvent and 2D material. Hence, the nanosheets tend to reaggregate if the dispersion in solvent is not stable. The schematic depicting acoustic cavitation is shown in figure S10.

Supplementary Note 6 – DFT Calculations

DFT Calculations were carried out to study the structural properties of monolayer, bilayer and trilayer TiS_2. The adsorption behavior at different sites of TiS_2 was also investigated as explained below.

Structural properties:

We considered trigonal (1T) and hexagonal (2H) crystallographic phases to understand the stability of these configurations. The structural parameters are optimized by varying the unit cell volume and atomic positions using the total energy and force convergence criteria. The

optimized structural parameters such as lattice parameter (a), bond length (Ti-S), vertical height (S-S) are listed in Table 3 and also compared with the reported literature results. The computed optimized structural parameters are in agreement with the reported literature values [3]. We noticed that the total energy of TiS_2-1T phase monolayer is 0.033 Ry smaller than that of TiS_2-2H phase monolayer. Thus, monolayer of TiS_2-1T phase is energetically more favorable than TiS_2-2H phase. This observation is in agreement with previous reports [4]. Further, TiS_2 bilayer and trilayer are derived from the bulk structure and optimized without any constraint. The optimized structures of monolayer, bilayers and trilayers are shown in Figure S18, with respective structural parameters such as height between layer, bond angle and bond length. In bilayer and trilayer TiS_2 structures, Van der Waals (vdW) distance between the monolayers is around 2.85Å, which is half of the bulk TiS_2 c axis.

Adsorption behavior

We investigated various sites on the TiS_2 monolayer, bilayer and also different orientations of the adsorbate gas molecules to investigate the sensing behavior of H_2S and O_2 gas molecules. The adsorption of gas molecule is considered on the top of the sulfur, titanium and hollow sites of hexagon. We also considered the adsorption of H_2S from both hydrogen and sulfur sites. The structures with adsorbate molecules are fully relaxed and the adsorption energy, Bader charge, charge difference density and density of states are computed to understand the sensing mechanism for each adsorbate molecule. The schematic view of all the considered geometries for H_2S and O_2 adsorbed on TiS_2 monolayer are shown in Figure S20 and Fig. S21, respectively. DFT-D2 correction is also considered to include vdW interaction between host and adsorbate gas molecule and also to compute the better adsorption energies. Adsorption energy is computed as $E_{ad} = E_{monolayer/bilayer+mo} - E_{monolayer/bilayer} - E_{mol}$; where,

$E_{monolayer/bilayer+mo}$ and $E_{monolayer/bilayer}$ are the total energy of gas molecule adsorbed monolayer or bilayer and pristine monolayer or bilayer, respectively and E_{mol} is the total energy of the gas molecule. Adsorption energy is used to find the most stable configuration of the adsorbed gas molecule on TiS_2 monolayer and bilayer. The more negative adsorption energy signifies the more favorable adsorption site.

The electrical conductivity of the semiconductor depends on the band gap of semiconductor material as $\sigma \propto e^{\frac{-E_g}{2KT}}$; where E_g, K and T are the band gap, Boltzmann constant and temperature in K, respectively. The recovery time τ of a sensor depends on the adsorption energy as $\tau \propto \exp\left(-\frac{E_{ad}}{KT}\right)$; E_{ad} is the adsorption energy. The charge transfer mechanism is considered as the main working mechanism in two-dimensional materials-based gas sensor. The adsorbate molecule may behave like a donor or acceptor and thus, receive or inject carrier from or to the host, leading to the charge transfer between adsorbate and host system.

Supplementary Note 7 – Physisorption

The physisorption here indicates that the adsorbate is attached to adsorbent with weak van der Waal's force of attraction. Since weak van der Waal's forces are involved, the enthalpy of adsorption is low and therefore adsorption is favorable at lower temperatures. The room temperature reversible operation of the Hydrogen Sulfide and Oxygen sensor observed in our work can be ascribed to physisorption based charge transfer. In one of the previous works reported by Ou et al, 2D SnS_2 based reversible and selective NO_2 gas sensor has been demonstrated. Here, the NO_2 gets physiosorbed onto 2D SnS_2 owing to the high physical affinity and favorable electronic band positions of the material. This sensor showed reversible response at lower temperature of 120^{o}C which is attributed to physisorption enabled charge transfer[5]. Hussain's group studied physisorption of H_2S and NH_3 on Lithium doped Graphene

sheet using first principle DFT calculations. They concluded that during this physisorption process, the adsorption energy decreases while going from single molecule to two molecules. Additionally, the work function was found to decrease while gas molecules reached closer to the Li doped graphene sheet, indicating the strong affinity of sheet towards the analyte molecules[6].

Supplementary Note 8 – Reversibility

Reversibility here refers to the complete recovery of the sensor to its original baseline value when the target gas (here H_2S and O_2) is taken off and reference gas (dry air) is purged. Additionally, the reversible switching behavior was observed when device was subjected to five consecutive cycles of 3 ppm H_2S. Our sensor demonstrates complete recovery at room temperature without any external energy like UV irradiation, red light or any ion beam irradiation [7] etc. For instance, Kumar et al. have demonstrated MoS_2 based reversible NO_2 gas sensor at room temperature. However, they have used thermal energy and photo excitation for the recovery of the sensor to the original baseline value[8]. Wu et al. have employed p-type $MoTe_2$ for reversible detection of NO_2 at room temperature. Here again, the recovery was done under UV illumination to develop a reversible sensor[9]. Therefore, Reversibility is one of the important parameters for a sensor to be deployed commercially for real time gas sensing applications. If the sensor does not recover, the sensing material will be poisoned with the adsorbed gaseous species and degrade rapidly over a period of time.

Supplementary Figures

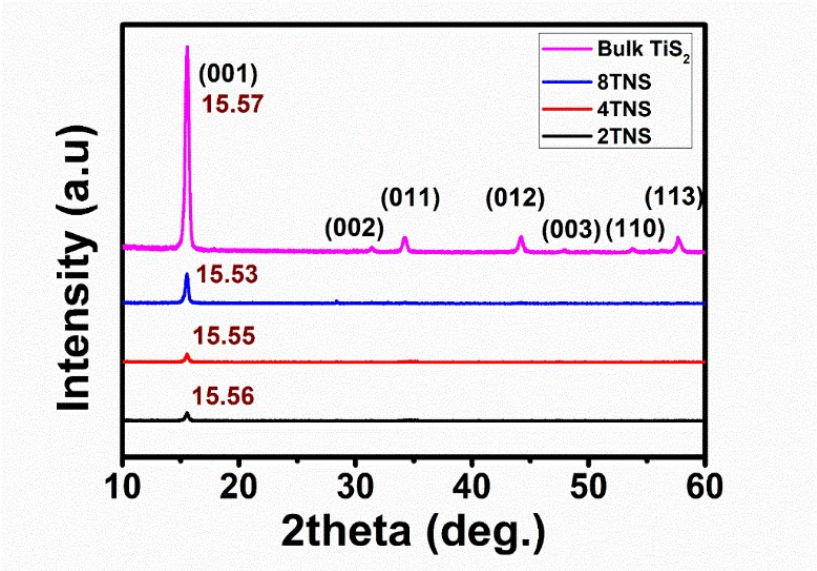

Figure S1. XRD pattern of 2TNS,4TNS,8TNS and bulk TiS_2

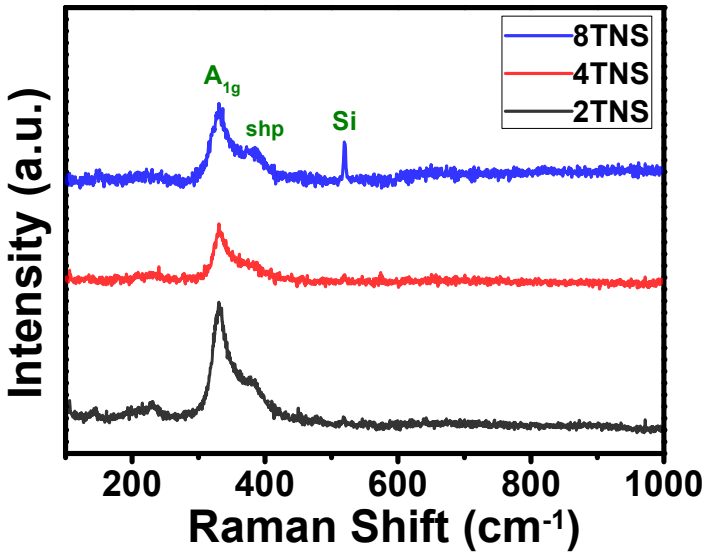

Figure S2. Raman Spectra of Specimen 2TNS,4TNS and 8TNS.

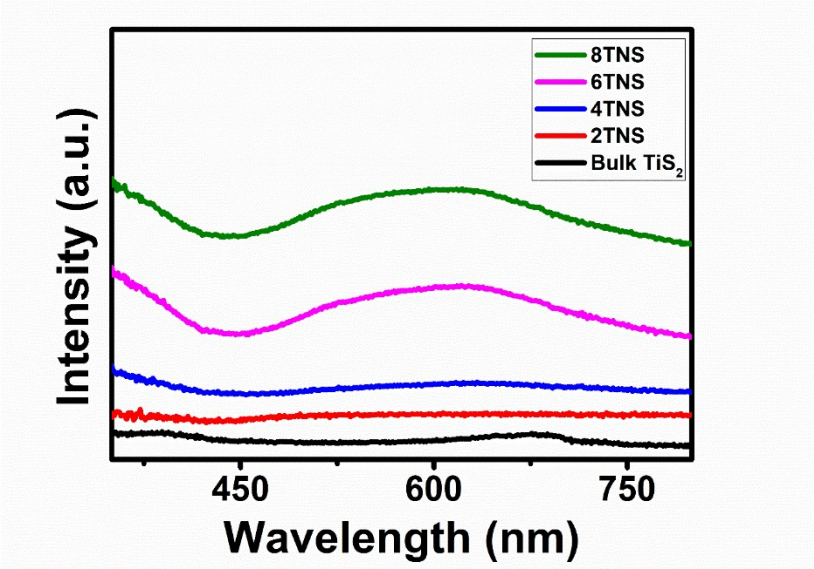

Figure S3. UV-Visible spectroscopies of 2TNS, 4TNS, 6TNS,8TNS and bulk TiS_2

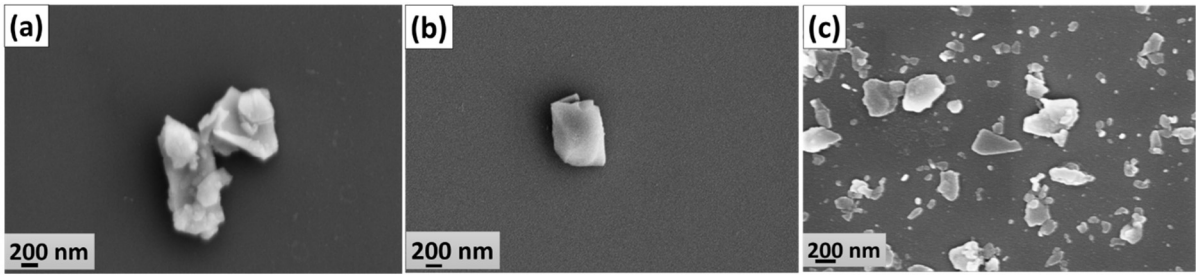

Figure S4. SEM Micrograph of specimen (a) 2TNS, (b) 4TNS and (c) 8TNS

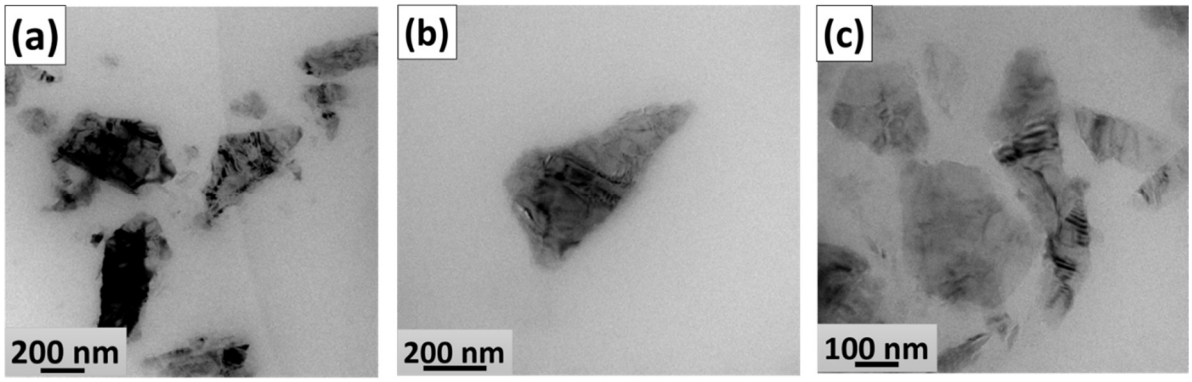

Figure S5. TEM Micrograph of specimen (a) 2TNS, (b) 4TNS and (c) 8TNS

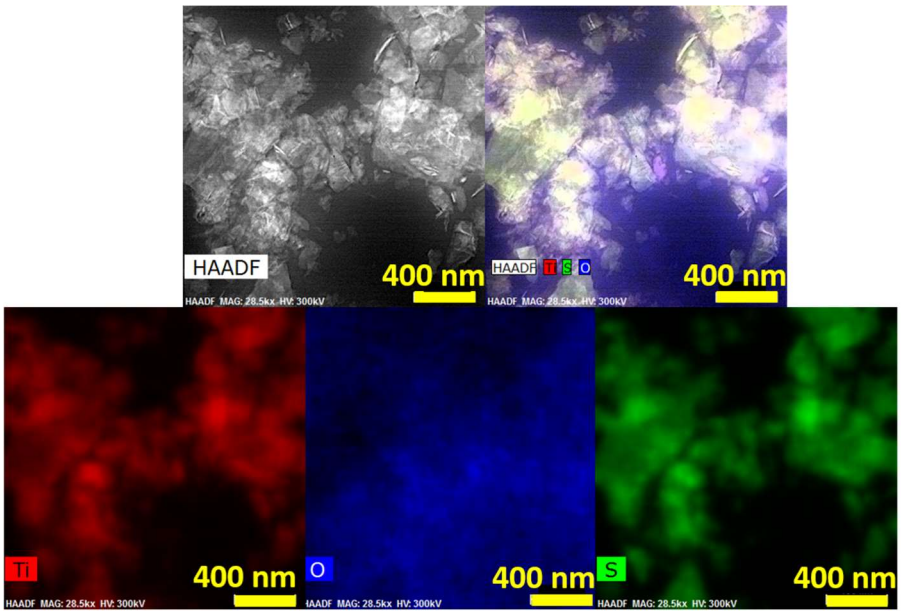

Figure S6. STEM HAADf spectral mapping images of 6TNS specimen

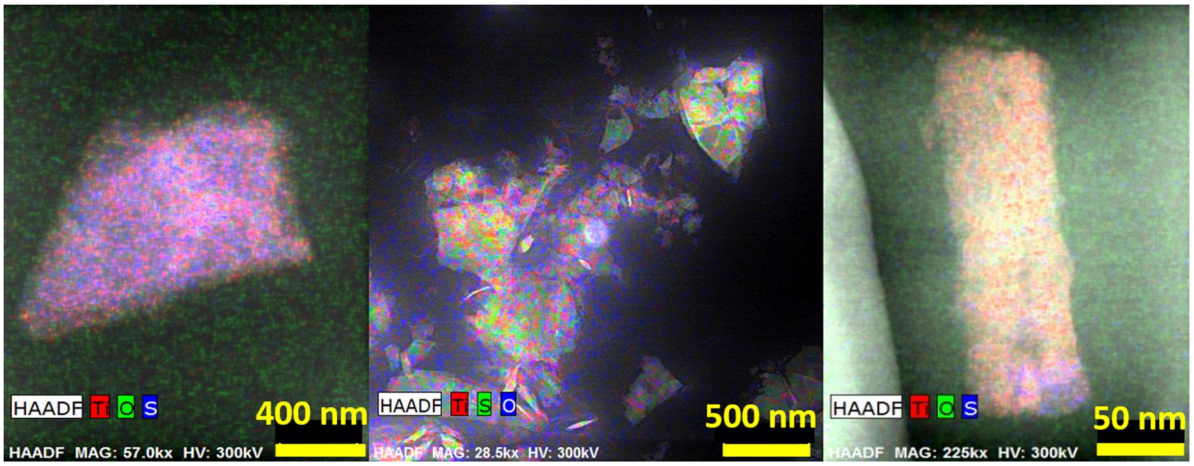

Figure S7. STEM HAADf spectral mapping images of (a) 2TNS (b) 4TNS and (c) 8TNS

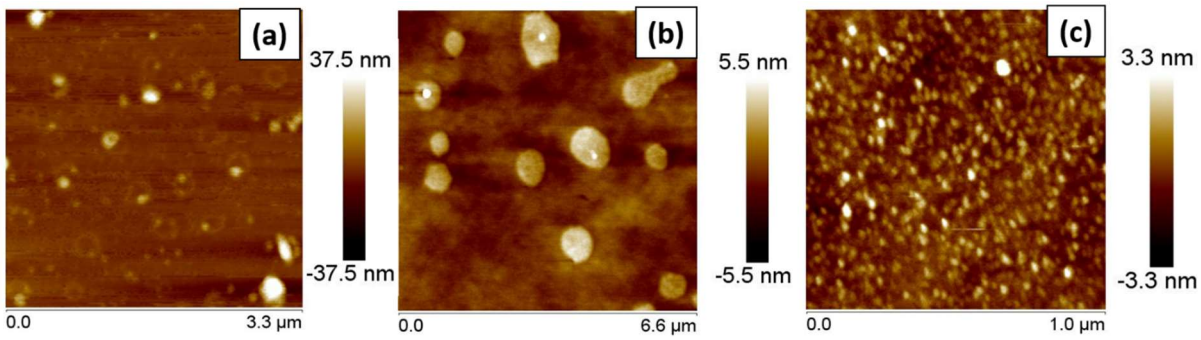

Figure S8. AFM Image of (a) 2TNS, (b) 4TNS and (c) 8TNS

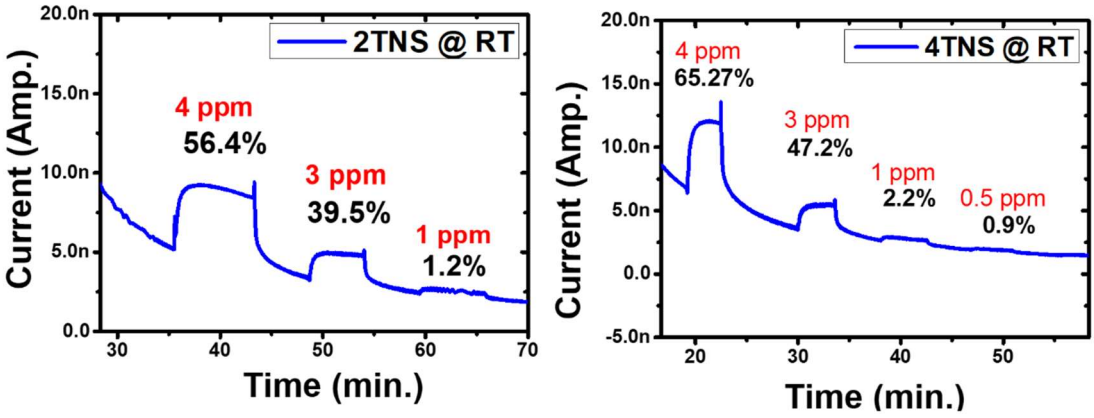

Figure S9. Dynamic Sensing plot towards H_2S for (a) 2TNS and (b) 4TNS at room temperature

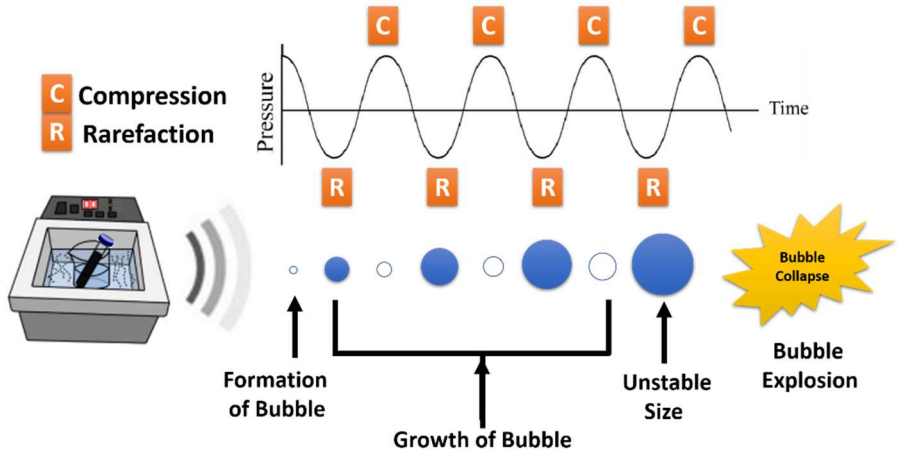

Figure S10. Schematic showing acoustic cavitation responsible for liquid exfoliation

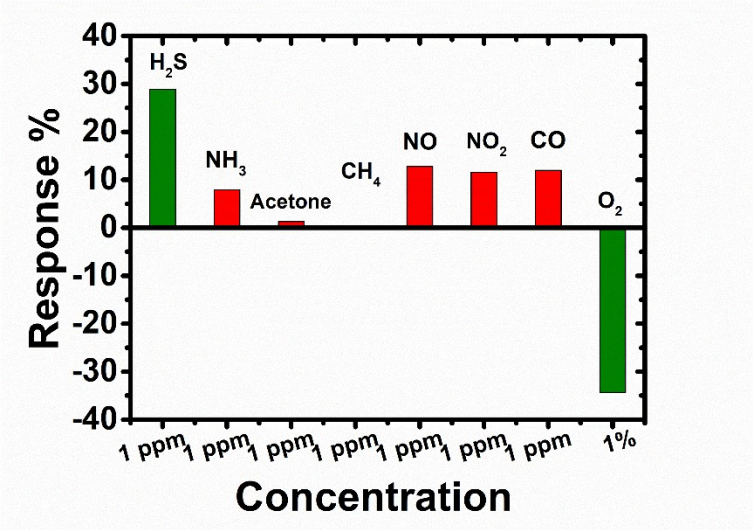

Figure S11. Histogram representing response % of 6TNS towards 1 ppm of different gases

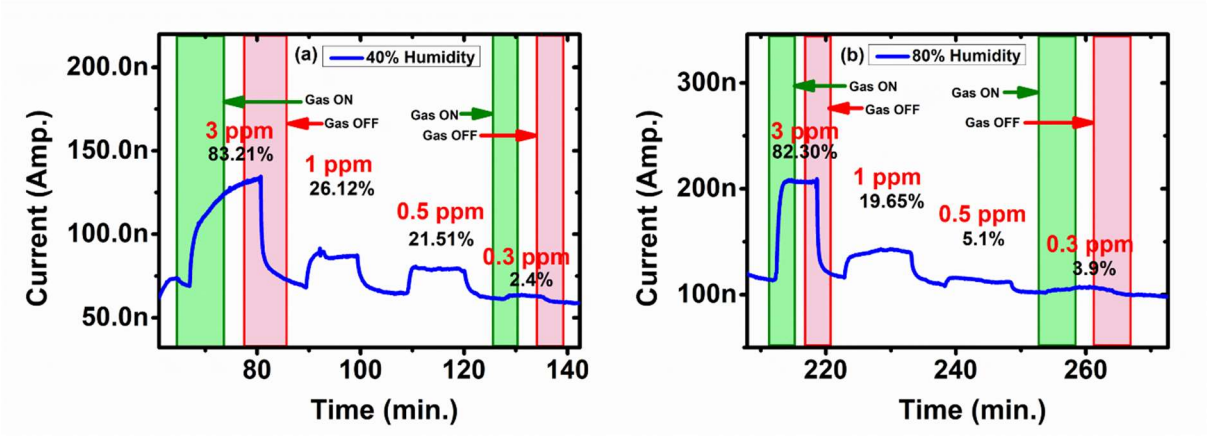

Figure S12. H_2S gas sensing in the presence of (a) 40% humidity and (b) 80% humidity.

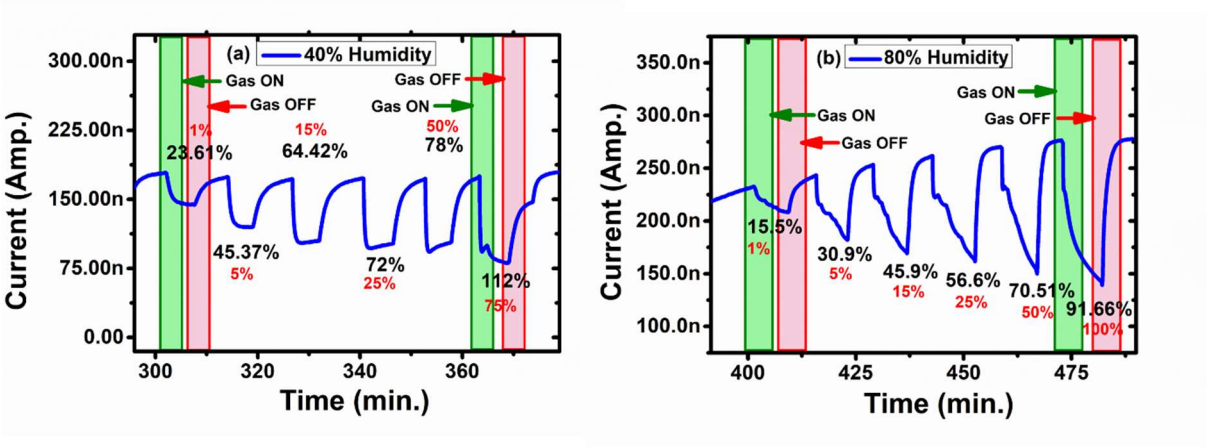

Figure S13. O_2 gas sensing in the presence of (a) 40% humidity and (b) 80% humidity.

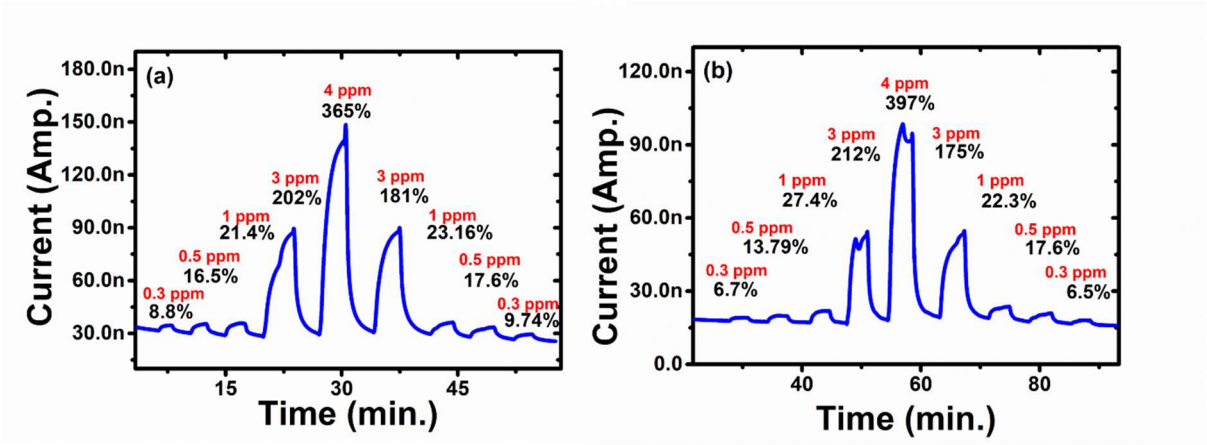

Figure S14. H_2S gas sensing of two different devices (a and b) depicting current variation from low to high concentration and vice-versa.

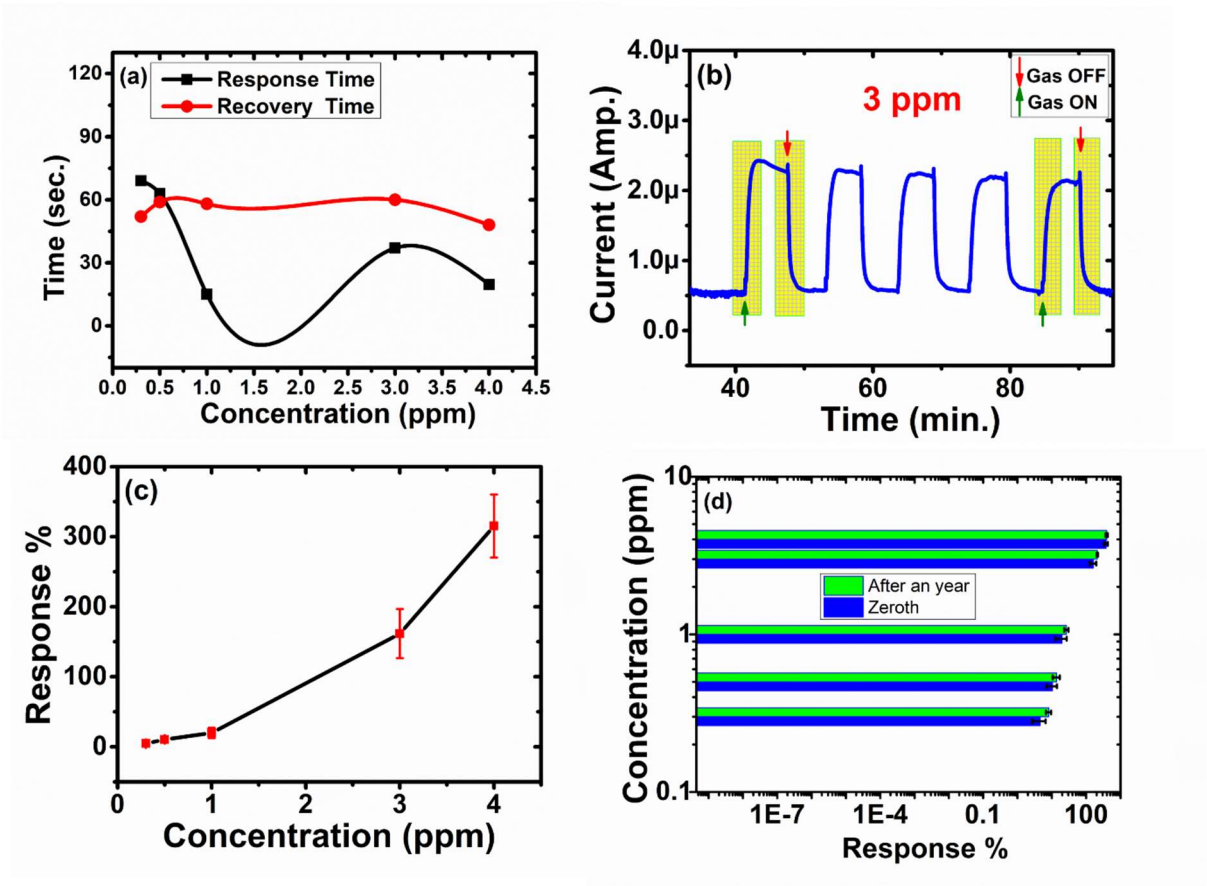

Figure S15 (a) Response time and recovery time for all conc. of H_2S, (b) Repeatability test at 3 ppm H_2S, (c) Inter device Variation and (d) Long term stability (computed using three different devices).

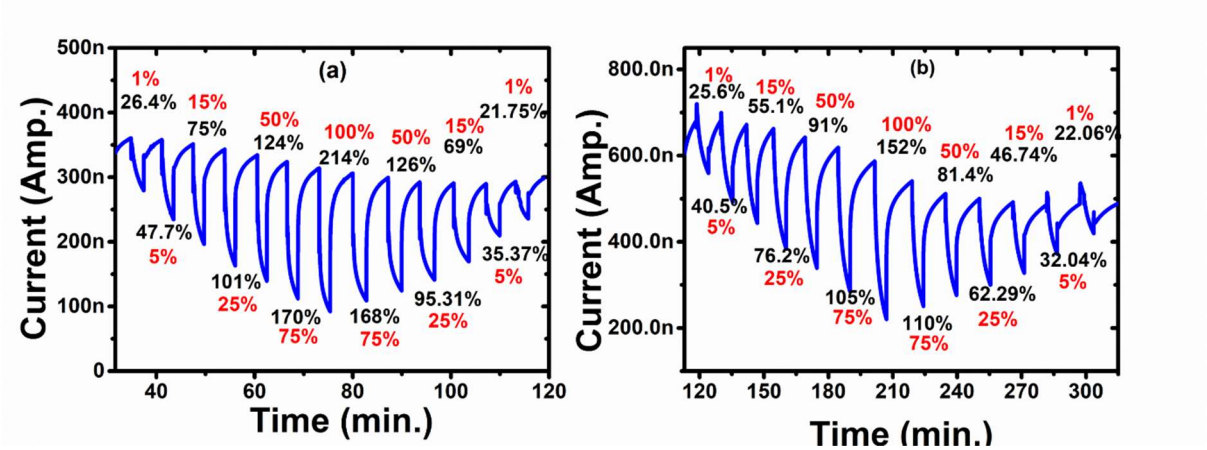

Figure S16. O_2 gas sensing of two different devices (a and b) depicting current variation from low to high concentration and vice-versa.

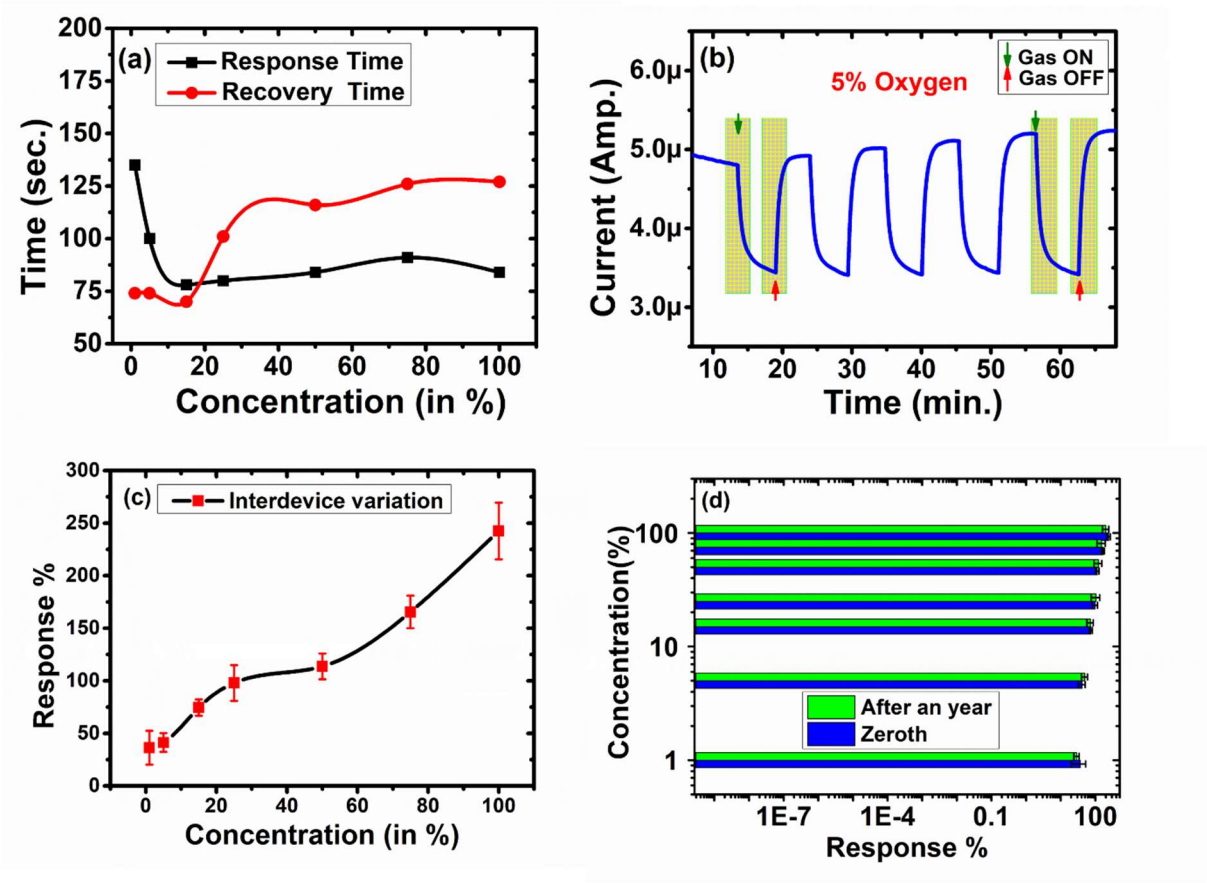

Figure S17. (a) Response time and recovery time for all conc. of Oxygen, (b) Repeatability test at 5% Oxygen, (c) Inter device Variation and (d) Long term stability (computed using three different devices)

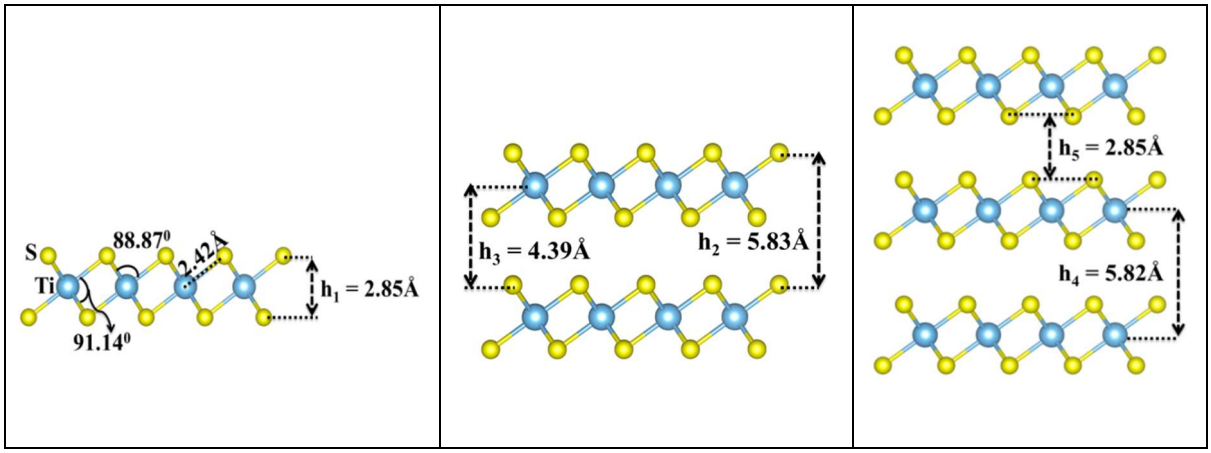

Figure S18. TiS_2 optimized structures for (a) monolayer (b) bilayer and (c) trilayer with respective structural parameters. (Here, yellow and sky-blue balls represent sulfur and titanium atom, respectively)

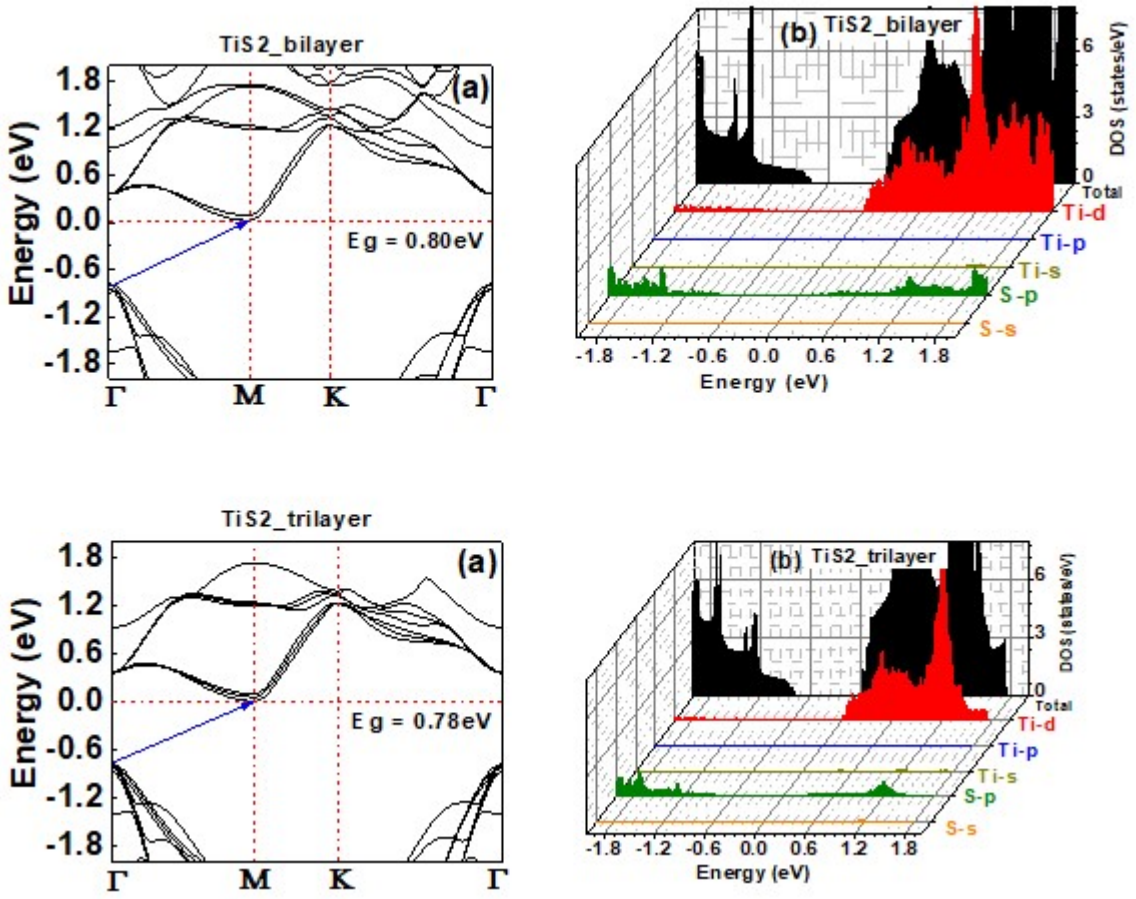

Figure S19. (a) Electronic band structure and (b) total and partial density of states of 1T-TiS_2 bilayer system and trilayer system.

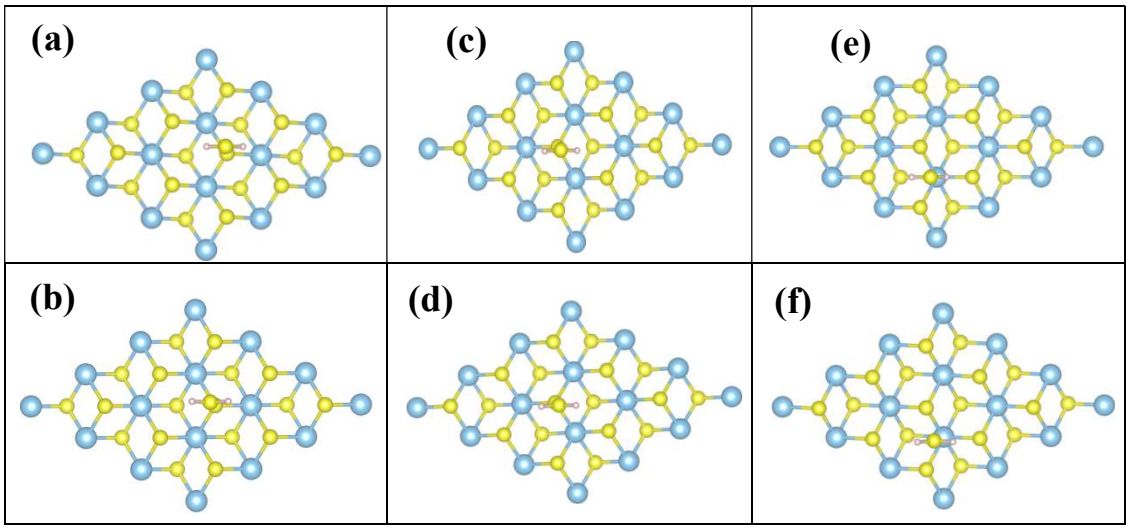

Figure S20: Schematic view of TiS_2 monolayer with H_2S adsorbate molecule from (a) the hydrogen site at top of sulfur atom, (b) the sulfur site at the top of sulfur atom, (c) the hydrogen site towards the hollow, (d) the sulfur site towards the hollow, (e) the hydrogen site at the top of titanium atom and (f) the sulfur site at the top of titanium atom.

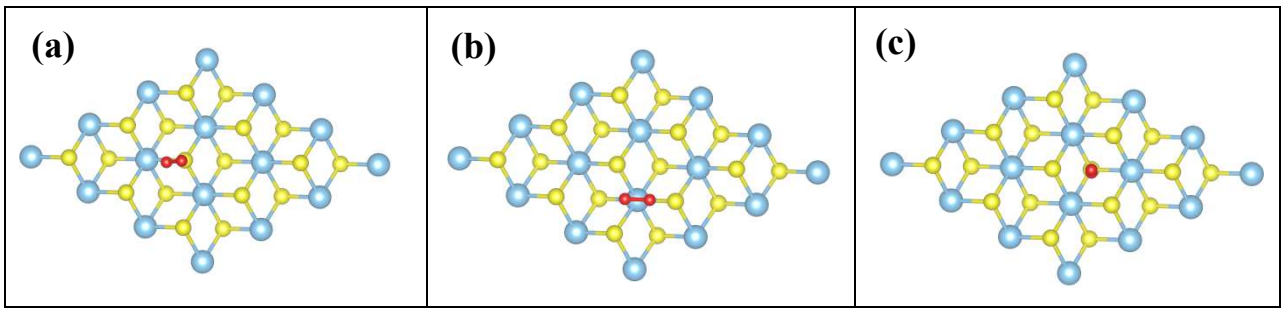

Figure S21. Schematic view of TiS_2 monolayer with O_2 adsorbate molecule (a) at top of sulfur atom, (b) at the top of the titanium atom and (c) at the hollow site

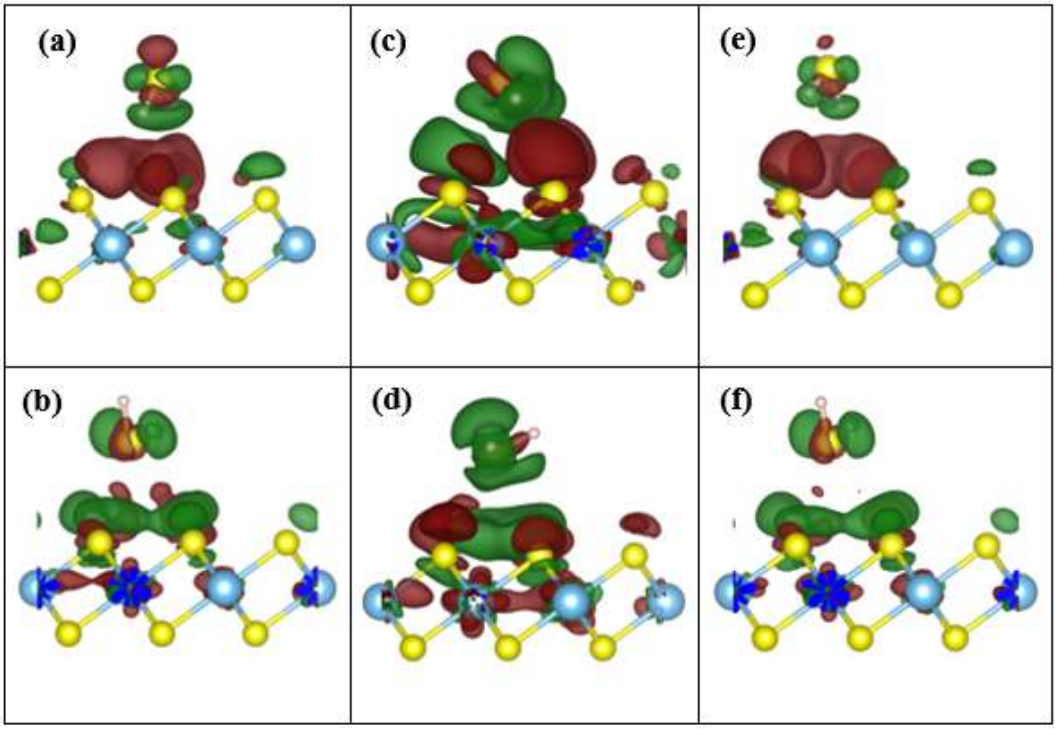

Figure S22. Charge difference density of H_2S molecule adsorbed from (a) the hydrogen site at top of sulfur atom, (b) the sulfur site at the top of sulfur atom, (c) the hydrogen site towards the hollow, (d) the sulfur site towards the hollow, (e) the hydrogen site at the top of titanium atom and (f) the sulfur site at the top of titanium atom (Wine color represents the charge accumulation and green color represents the charge depletion)

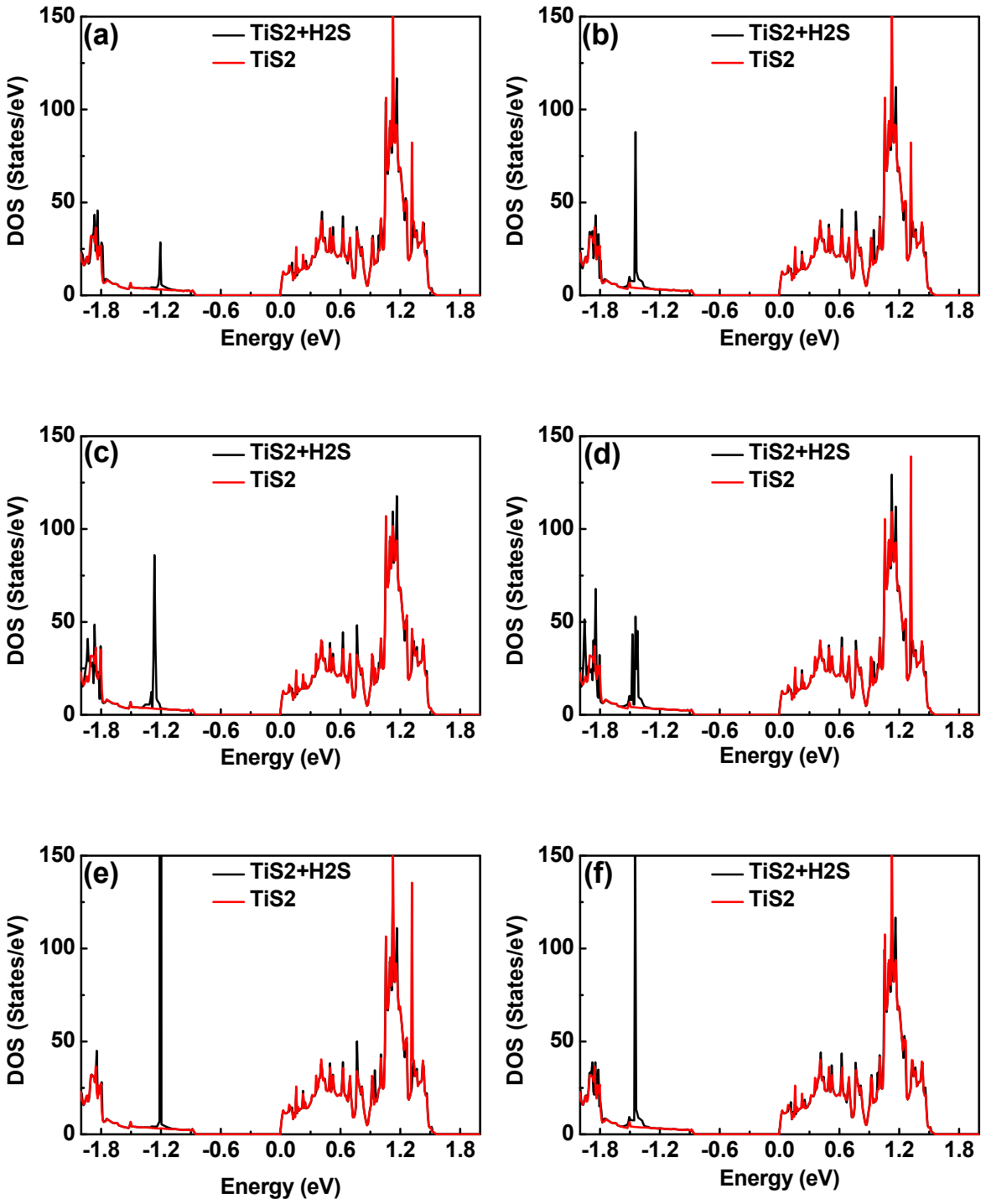

Figure S23 : Density of states of H_2S molecule adsorbed from (a) the hydrogen site at top of sulfur atom, (b) the sulfur site at the top of sulfur atom, (c) the hydrogen site towards the hollow, (d) the sulfur site towards the hollow, (e) the hydrogen site at the top of titanium atom and (f) the sulfur site at the top of titanium atom.

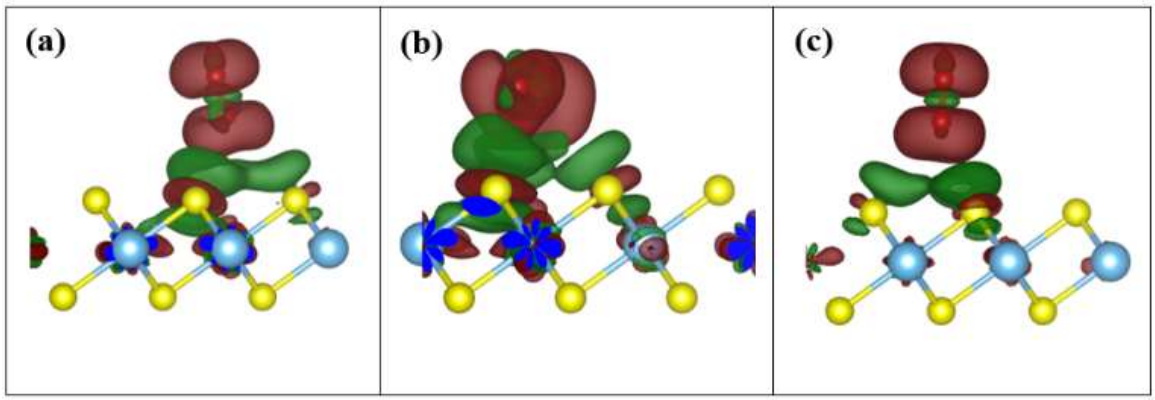

Figure S24. Charge difference density of (a) O_2 adsorbed at top of sulfur atom, (b) O_2 adsorb at the top of the titanium atom and (c) O_2 adsorbed at the hollow site (Wine color represents the charge accumulation and green color represents the charge depletion)

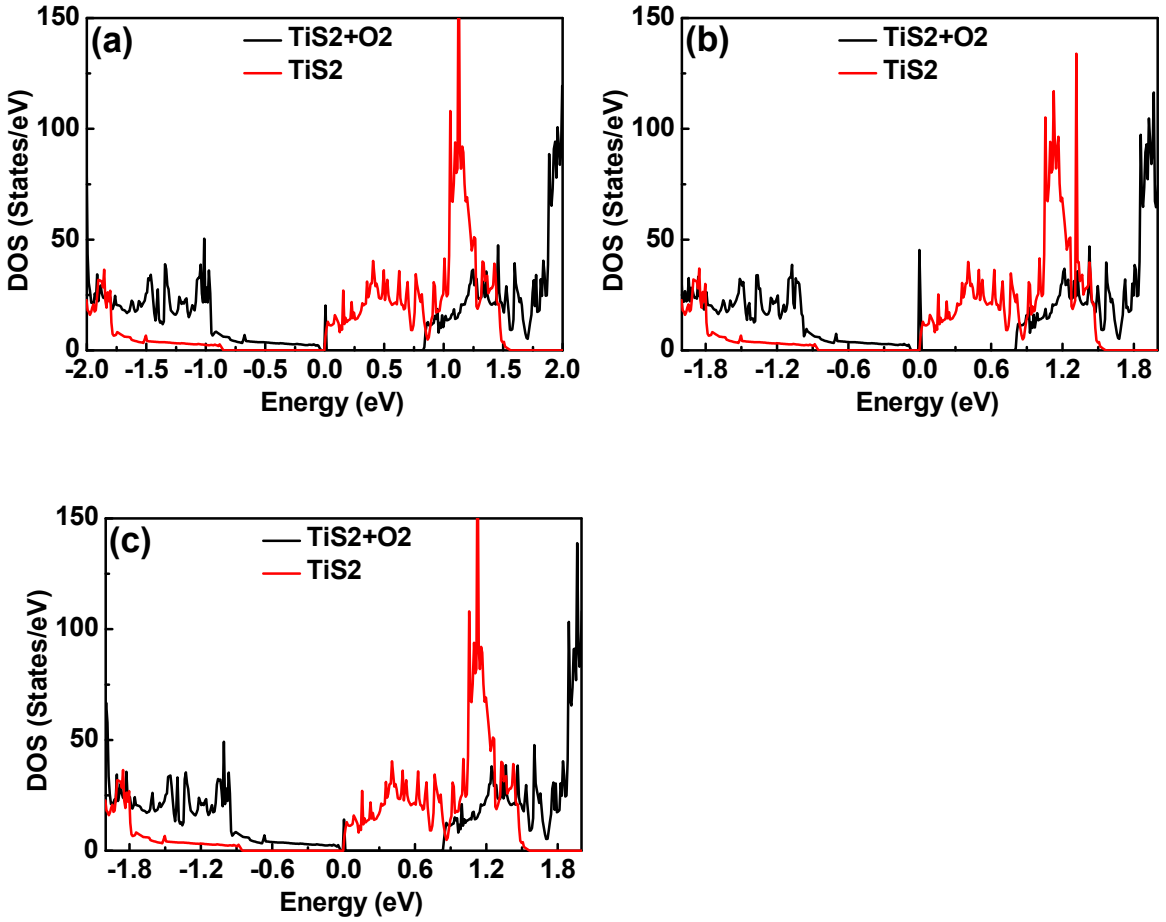

Figure S25: Density of states of (a) O_2 adsorbed at top of sulfur atom, (b) O_2 adsorb at the top of the titanium atom and (c) O_2 adsorbed at the hollow site

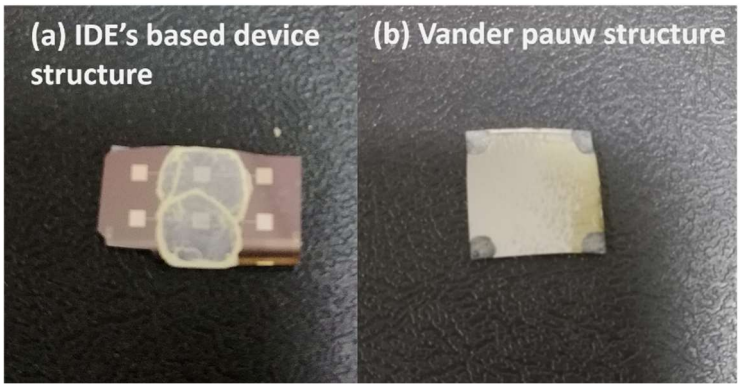

Figure S26. (a) Interdigitated device structure patterned on Si/SiO_2 substrate with drop casted TiS_2 nanosheets and (b) vander pauw structure on silicon substrate

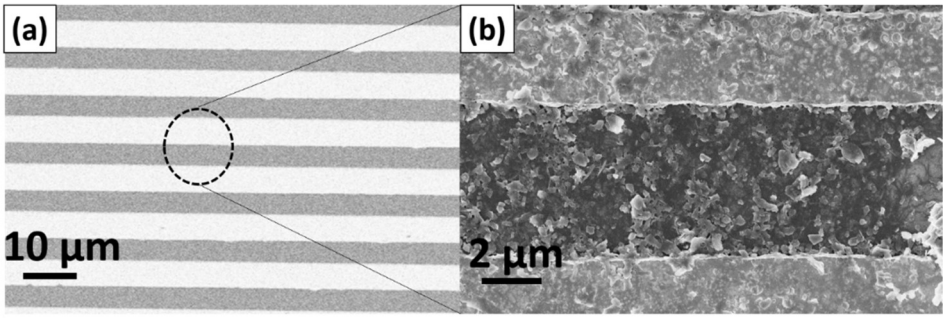

Figure S27. Inter-digitated Electrodes (a) without material (b) Magnified view with drop casted material

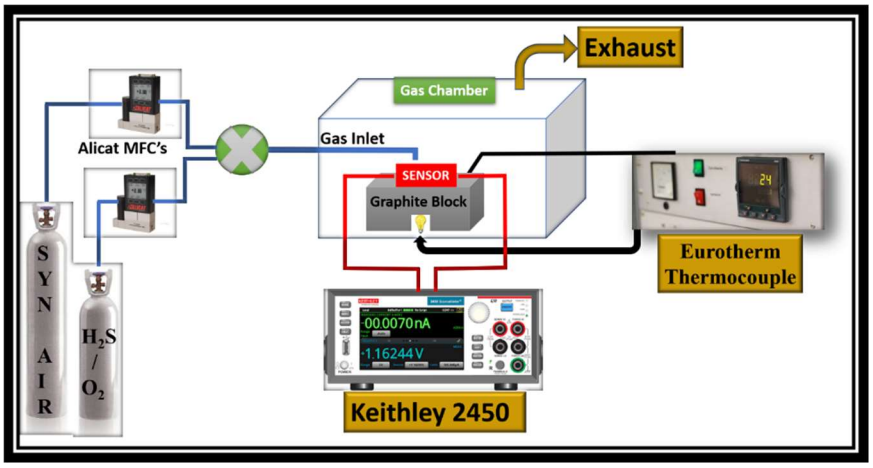

Figure S28. In-house built Gas Sensing Set up

Table S3: Comparison of our H_2S sensor with reports in Literature

S.No.	Material	Response (%)	Response Time/ Recovery Time (Seconds)	Operating Temperature (°C)	LOD (ppb)	Ref.
1	Pt-SnO_2	60% @ 0.1ppm	192.4/76.5 @ 1 ppm	250	0.1 ppm (0.1 – 5 ppm)	[10]
2	rGO/WO_3	980% @ 10 ppb	15/70 @ 10 ppm	330	10ppb (10 ppb – 40 ppm)	[11]
3	WS_2	2.3@ 1 ppm	-----	200	(20 ppb) 20 ppb – 1ppm	[12]
4	SnO_2/ZnO	175% @ 10 ppb	/513 @ 5ppm	100	10 ppb (10 ppb – 10 ppm)	[13]
5	α-Fe_2O_3	30% @ 50 ppb	30/5 @ 10 ppm	300	50 ppb (50 ppb – 10 ppm)	[14]
6	PANI nanowires/Au nanoparticles	20% @ 0.1 ppb	120/300	RT	0.1 ppb (0.1 ppb – 1 ppm)	[15]
7	SWCNT/Au	6% @ 20 ppb	480/1200	RT	3 ppb (20 ppb – 1000 ppb)	[16]
8	Fe_2O_3/Au Film	538% @10 ppm	99/1620	250	1 ppm (1-50 ppm)	[17]
9	Fe doped SnO_2 nanoparticles	45% @10 ppm	5-10/95-105 @ 50 ppm	RT	10 ppm (10-50 ppm)	[18]
10	CuO-SnO_2 film	40% @20 ppb	1200/- @ 20 ppb	300	20ppb (20 ppb – 10 ppm)	[19]
11	SnO_2 nanowire/RGO	50% @ 10 ppm	2/292	RT	10 ppm (10-100 ppm)	[20]
12	In_2O_3	50% @ 20 ppb	1800/300	RT	20 ppb (20ppb - 20 ppm)	[21]
13	CuO NW	57% @ 10 ppb	------	325	10 ppb (10ppb-500 ppb)	[22]
14	$ZnFe_2O_4$ NF/RGO	460% @ 100 ppb	<10/~500@ 1 ppm	350	100 ppb (100ppb to 1 ppm)	[23]
15	Fe_2O_3 Ellipsoids	120% @ 100 ppb	0.8/2.2 @ 50 ppm	260	100 ppb (100 ppb – 400 ppm)	[24]
16	SnO_2/RGO/ PANI NC	3.18% @50 ppb	82/78 @ 2 ppm	RT	50 ppb (50 ppb-1 ppm)	[25]
17	CuO NP	3.5% @ 0.2 ppb	200/1000	293 K (19.85degC)	0.2 ppb (0.2 ppb- 1 ppm)	[26]
18	CdS decorated NiO nanofilm	104% @ 0.5 ppb	----	92	0.5 ppb (0.5 – 100 ppb)	[27]
19	ZnO nanorod bundles	3800% @ 50ppm	300/250 @ 50 ppm	500	50 ppm	[28]
20	Au functionalized ZnO nanowires	3700% @ 1ppm	-/170 @ 5 ppm	RT	1 and 5 ppm	[29]
21	ZnO nanowire (20 nm)	4% @ 5 ppb	258/882 @ 50 ppb	300	5 ppb (5 ppb – 200 ppb)	[30]
22	ZnO/CuO Nanowire network	1400% @ 500 ppb	360/1800 @ 5ppm	200	0.5 ppm (0.5 – 30 ppm)	[31]
23	ZnO nanowire	2% @ 50 ppb	180/60 @ 2 ppm	150	20 ppb (50 ppb – 5 ppm)	[32]
24	ZnO nanowire/Cobalt	69% @ 5 ppm	26/175 @ 10 ppm	RT	1 ppm (5 – 50 ppm)	[33]

	Phthalocyanine Heterojunction					
25	Cu doped ZnO nanofibers	75% @ 1 ppm	18/20 @ 10 ppm	230	1 ppm (1 ppm – 10 ppm)	[34]
26	ZnO microsphere	280% @ 50 ppb	219/227 @500 ppb	220	50 ppb (50 – 1000 ppb)	[35]
27	ZnO nanorod (spray pyrolysis)	400% @ 5 ppm	50/20 @ 5 ppm	RT	5 ppm (5 ppm – 500 ppm)	[36]
28	CuO functionalized ZnO tetrapods	8% @ 5 ppm	-/5000 @ 50 ppm	50	5 ppm (5 – 100 ppm)	[37]
29	ZnO hollow tubules	600% @ 10 ppb	61/59 @ 10 ppb	217	10 ppb (10 ppb to 1000 ppb)	[38]
30	ZnO-CuO	8.6% @ 10 ppb	78/70	125	10 ppb (10 ppb – 10 ppm)	[39]
31	W-WO3	387.7% @ 10 ppb	12 /19 @ 1ppm	150	10 ppb (10 ppb – 1 ppm)	[40]
	TiS_2	7.4% @ 300 ppb	19.87/48 @ 4 ppm	RT	300 ppb (300 ppb- 4 ppm)	Our work

Table S4 – Comparison of our Oxygen sensor with reports in Literature

Sl. No	Material	Response%	Response/Recovery Time	Operating Temperature	LLOD (Concentration Range)	Reference
1	Pt-In_2O_3	6230% @ 20%	50/40s	200	2.5% (2.5% to 20%)	[41]
2	ZnO	5000% @ 97%	<300s/<500s	200	97% (only 97%)	[42]
3	TiO_2	7000% @ 1.8%	500s/300s	100C	200 ppm (200 ppm-20%)	[43]
4	STFO	356% @ 1%	2.1/135s	700C	1% (1% to 20%)	[44]
5	$SrTiO_3$	100% @ 20%	96/300s	40C	20%	[45]
6	Graphene/TiO_2	7% @ 134 ppm	193/135s	RT/UV assisted	134 ppm (134 ppm - 100%)	[46]
7	MWCNTs/PVAc /TiO_2	3000% @ 5%	<100s/<120s	400C	5% (5% to 20%)	[47]
8	ZnO	9.5% @ 20%	3500/4500s	RT	20% (only 20%)	[48]
9	MoS_2	869% @ 2%	<300s/<500s	300C	2% (2% - 100%)	[49]
10	TiO_2	15% @ 1%	50s/60s	RT	1% to 16%	[50]
11	TiS_2	5% @ 20%	720s/--	50	15% to 20%	[51]
12	SnO_2	13% @ 20%	1800s/1800s	RT	Only 20%	[52]
13	$CuAlS_2$	15% @ 20%	92.4s/120s	RT	Only 20%	[53]
14	$CuFeTe_2$	0.88% @ 20%	54 s/600-1200s	RT	20% and 100%	[54]

15	Pt-In_2O_3	95% @ 20%	1080s/2100s	RT	5% 20to 20%	[55]
13	TiS_2	34.8% @ 1%	78/70s for 15% oxygen	RT	1%	Our work

Table S5 – Comparison of the structural parameters of 1T and 1H TiS_2 phases

Structural parameters	Our results		Reported results	
	1T-TiS_2	**1H-TiS_2**	**1T-TiS_2**	**1H-TiS_2**
a	3.3973Å	3.3328 Å	3.35[a], 3.40[b], 3.41[c], 3.42[d] Å	3.33[b] Å
c	15 Å	15 Å		
d	2.426 Å		2.40[a], 2.43[d] Å	2.45[b] Å
h	2.856 Å		2.83[d], 2.84[e], 2.85[d] Å	
Band gap	0.85 eV		0.48[c], 0.62[b], 1.12[c] eV	
Total energy	-316.5985428 Ry	-316.56586107 Ry		

h = Vertical distance (S-S), d = bond length (Ti-S)

[a]Ref. [56], [b]Ref. [57], [c]Ref. [2], [d]Ref. [58], [e]Ref.[59]

References

1. Auluck, S. and Reshak, A. H. Electronic and Optical Properties of the 1T Phases of TiS2, TiSe2, and TiTe2. Phys. Rev. B, 68, 245113−245120 (2003).
2. Qiao, Wen, et al. "Effects of ultrasonic cavitation intensity on the efficient liquid-exfoliation of MoS2 nanosheets." Rsc Advances 4.92, 50981-50987 (2014).
3. Cucinotta, Clotilde S., et al. Two-dimensional transition metal dichalcogenide monolayers as promising sodium ion battery anodes. *The Journal of Physical Chemistry C* 119, 27 ,15707-15715 (2015).
4. Samad, Abdus, Aamir Shafique, and Young-Han Shin. "Adsorption and diffusion of mono, di, and trivalent ions on two-dimensional TiS2." Nanotechnology 28 (17), 175401 (2017).
5. Ou, Jian Zhen, et al. "Physisorption-based charge transfer in two-dimensional SnS2 for selective and reversible NO2 gas sensing." ACS nano 9(10), 10313-10323 (2015).
6. Hussain, Tanveer, Puspamitra Panigrahi, and Rajeev Ahuja. "Enriching physisorption of H 2 S and NH 3 gases on a graphane sheet by doping with Li adatoms." Physical Chemistry Chemical Physics 16(17), 8100-8105 (2014).
7. Kwon, Yong Jung, et al. "Selective improvement of NO2 gas sensing behavior in SnO2 nanowires by ion-beam irradiation." ACS applied materials & interfaces 8(21),13646-13658 (2016).
8. Kumar, Rahul, Neeraj Goel, and Mahesh Kumar. "UV-activated MoS2 based fast and reversible NO2 sensor at room temperature." ACS sensors 2(11),1744-1752 (2017).

9. Wu, Enxiu, et al. "Ultrasensitive and Fully Reversible NO2 Gas Sensing Based on p-Type MoTe2 under Ultraviolet Illumination." ACS sensors 3(9), 1719-1726 (2018).
10. Bulemo, P. M. *et al.* Facile Synthesis of Pt-Functionalized Meso/Macroporous SnO2 Hollow Spheres through in Situ Templating with SiO2 for H2S Sensors. ACS Applied Materials & Interfaces, 10, 18183-18191 (2018).
11. Shi, J. *et al.* Facile synthesis of reduced graphene oxide/hexagonal WO3 nanosheets composites with enhanced H2S sensing properties. Sensors and Actuators B: Chemical, 230, 736-745 (2016).
12. Asres, G. A. *et al*. Ultrasensitive H2S gas sensors based on p-type WS2 hybrid materials. Nano Research, 11, 4215-4224 (2018).
13. Fu, D. *et al.* Two-dimensional net-like SnO2/ZnO heteronanostructures for high-performance H 2 S gas sensor. Journal of Materials Chemistry A, 4, 1390-1398 (2016).
14. Li, Z. *et al*. A fast response & recovery H2S gas sensor based on α-Fe2O3 nanoparticles with ppb level detection limit. Journal of Hazardous Materials, 300, 167-174 (2015).
15. Shirsat, M. D. *et al.* A. Polyaniline nanowires-gold nanoparticles hybrid network based chemiresistive hydrogen sulfide sensor. Applied Physics Letter, 94, 083502 (2009).
16. Mubeen, S. *et al.* Sensitive Detection of H2S Using Gold Nanoparticle Decorated Single-Walled Carbon Nanotubes. Analytical Chemistry, 82, 250-257 (2010).
17. Balouria, V. *et al.* Enhanced H2S sensing characteristics of Au modified Fe2O3 thin films. Sensors and Actuators B: Chemical, 219, 125-132 (2015).
18. Vaishampayan, M. V. *et al.* Fe-doped SnO2 nanomaterial: A low temperature hydrogen sulfide gas sensor. Materials Chemistry and Physics, 109, 230-234 (2008).
19. Tamaki, J. *et al.* Dilute hydrogen sulfide sensing properties of CuO–SnO2 thin film prepared by low-pressure evaporation method. Sensors and Actuators B: Chemical, 49, 121-125 (1998).
20. Song, Z. *et al.* Sensitive room-temperature H2S gas sensors employing SnO2 quantum wire/reduced graphene oxide nanocomposites. Chemistry of Materials 2016, 28, 1205-1212.
21. Yao, Kun et al. Parts per billion-level H2S detection at room temperature based on self-assembled In2O3 nanoparticles. *The Journal of Physical Chemistry C* 113,.33, 14812-14817 (2009).
22. Steinhauer S. et al. suspended CuO nanowires for ppb level H2S sensing in dry and humid atmosphere.*Sensors and Actuators B: Chemical* 186, 550-556 (2013).
23. Van Hoang Nguyen, et al. Excellent detection of H2S gas at ppb concentrations using ZnFe2O4 nanofibers loaded with reduced graphene oxide." *Sensors and Actuators B: Chemical* 282,876-884 (2019).
24. Wu, Zhonglin et al. Ultrafast Response/Recovery and High Selectivity of H2S Gas Sensor Based on α-Fe2O3 Nano-Ellipsoids from One-Step Hydrothermal Synthesis. *ACS applied materials & interfaces,* 11, 12761–12769 (2019).
25. Zhang, Dongzhi, Zhenling Wu, and Xiaoqi Zong. Flexible and highly sensitive H2S gas sensor based on in-situ polymerized SnO2/rGO/PANI ternary nanocomposite with application in halitosis diagnosis. *Sensors and Actuators B: Chemical ,*289, 32-41 (2019).
26. Li, Dengji et al. Ultra-highly sensitive and selective H2S gas sensor based on CuO with sub-ppb detection limit. *International Journal of Hydrogen Energy* ,44.7,3985-3992 (2019).
27. Yu, Ting-ting et al. Low concentration H2S detection of CdO-decorated hierarchically mesoporous NiO nanofilm with wrinkle structure. *Sensors and Actuators B: Chemical*,230, 706-713 (2016).

28. Kim, J. and Yong, K. Mechanism study of ZnO nanorod-bundle sensors for H2S gas sensing. The Journal of Physical Chemistry C, 115, 7218-7224 (2011).
29. Ramgir, N. S. *et al.* K. Room temperature H2S sensor based on Au modified ZnO nanowires. Sensors and Actuators B: Chemical, 186, 718-726 (2013).
30. Chen, Y. *et al*. ZnO-nanowire size effect induced ultra-high sensing response to ppb-level H2S. Sensors and Actuators B: Chemical, 240, 264-272 (2017).
31. Datta, N. *et al.* K. Selective H2S sensing characteristics of hydrothermally grown ZnO-nanowires network tailored by ultrathin CuO layers. Sensors and Actuators B: Chemical, 166-167, 394-401 (2012).
32. Huang, H. *et al.* Sulfuration–desulfuration reaction sensing effect of intrinsic ZnO nanowires for high-performance H2S detection. Journal of Materials Chemistry A, 3, 6330-6339 (2015).
33. Kumar, A. *et al*. K. Fast Response and High Sensitivity of ZnO Nanowires—Cobalt Phthalocyanine Heterojunction Based H2S Sensor. ACS Applied Materials & Interfaces, 7, 17713-17724, (2015).
34. Zhao, M. *et al.* Electrospun Cu-doped ZnO nanofibers for H2S sensing. Sensors and Actuators B: Chemical, 156, 588-592, (2011).
35. Diao, K. *et al*. High response to H2S gas with facile synthesized hierarchical ZnO microstructures. Sensors and Actuators B: Chemical, 219, 30-37 (2015).
36. Mani, G. K. and Rayappan, J. B. B. Selective recognition of hydrogen sulfide using template and catalyst free grown ZnO nanorods. RSC Advances,5, 54952-54962 (2015).
37. Kaur, Manmeet, *et al.* Selective H2S detection by CuO functionalized ZnO nanotetrapods at room temperature. *Materials Chemistry and Physics* 143,3, 1319-1324 (2014).
38. Na, Hui-Bing, *et al.* Large-scale synthesis of hierarchically porous ZnO hollow tubule for fast response to ppb-level H2S gas. *ACS applied materials & interfaces,* 12, 11627-11635 (2019).
39. Guo, Yanan, et al. Sensitive, selective, and fast detection of ppb-Level H 2 S gas boosted by ZnO-CuO mesocrystal." *Nanoscale research letters* 11,1, 475 (2016).
40. Benedict, Samatha, and Navakanta Bhat. Nanodisc decorated W-WOx suspended nanowire: A highly sensitive and selective H2S sensor. *IEEE Sensors Journal*, 6, 2023-2030 (2018).
41. G. Neri *et al.* In2O3 and Pt-In2O3 nanopowders for low temperature oxygen sensors, *Sensors Actuators, B Chem.*, 127,2,455–462 (2007).
42. C. S. Chou, Y. C. Wu, and C. H. Lin,High performance oxygen sensor utilizing ultraviolet irradiation assisted ZnO nanorods under low operation temperature, *8th Annu. IEEE Int. Conf. Nano/Micro Eng. Mol. Syst. IEEE NEMS*, 4,72–75 (2013).
43. H. F. Lu *et al.*, Amorphous TiO_2 nanotube arrays for low-temperature oxygen sensors, *Nanotechnology*,19,40, 405504 (2008).
44. S. H. Choi *et al.* Facile Synthesis of p-type Perovskite SrTi0.65Fe0.35O3-δNanofibers Prepared by Electrospinning and Their Oxygen-Sensing Properties, *Macromol. Mater. Eng.*, 298, 5, 521–527 (2013).
45. Y. Hu *et al.* "A New Form of Nanosized SrTiO 3 Material for Near-Human-Body Temperature Oxygen Sensing Applications," *J. Phys. Chem. B*,108,11214–11218 (2004).
46. J. Zhang *et al.* A UV light enhanced TiO2/graphene device for oxygen sensing at room temperature, *RSC Advances,* 3,44,22185 (2013).
47. P. Frontera *et al.* Oxygen-sensing properties of electrospun CNTs/PVAc/TiO2 composites, *Electron. Mater. Lett.*,10,1,305–313 (2014).
48. F. Chaabouni *et al.* Metrological characteristics of ZNO oxygen sensor at room temperature," *Sensors Actuators, B Chem.*,100,1–2,200–204 (2004).

49. Kim, Yeon Hoo, *et al*. Ultrasensitive reversible oxygen sensing by using liquid-exfoliated MoS2 nanoparticles. *Journal of Materials Chemistry A* 4,16,6070-6076 (2016).
50. Wang, Hairong, et al. A room temperature oxygen gas sensor based on hierarchical TiO2, *IEEE International Conference on Manipulation, Manufacturing and Measurement on the Nanoscale (3M-NANO)*, 199-202 (2016).
51. Kishiro, Koichi, et al. Resistivity response to oxygen of transition metal dichalcogenide TiS2. Japanese journal of applied physics 33(2R), 1069 (1994).
52. Atkinson, J., Cranny, A., & de Cloke, C. S. A low-cost oxygen sensor fabricated as a screen-printed semiconductor device suitable for unheated operation at ambient temperatures. Sensors and Actuators B: Chemical 47(1-3), 171-180 (1998).
53. Abaab, M., Bouazzi, A. S., & Rezig, B. Competitive CuAlS2 oxygen gas sensor. Microelectronic Engineering 51, 343-348 (2000).
54. Kishiro, K., Kuriyaki, H., & Hirakawa, K. Grain size effect of CuFeTe2 response to oxygen. Japanese journal of applied physics 32(5A), L674 (1993).
55. Neri, G., Bonavita, A., Micali, G., Rizzo, G., Galvagno, S., Niederberger, M., & Pinna, N. A highly sensitive oxygen sensor operating at room temperature based on platinum doped In2O3 nanocrystals. Chemical communications 48, 6032-6034 (2008).
56. Yang, Eunjeong, Hyunjun Ji, and Yousung Jung. Two-dimensional transition metal dichalcogenide monolayers as promising sodium ion battery anodes. *The Journal of Physical Chemistry C* 119, 47 26374-26380 (2015).
57. Samad, Abdus, Aamir Shafique, and Young-Han Shin. Adsorption and diffusion of mono, di, and trivalent ions on two-dimensional TiS2. *Nanotechnology 28*,17,175401 (2017).
58. Qu, Yuanju, Hui Pan, and Chi Tat Kwok. Hydrogenation-controlled phase transition on two-dimensional transition metal dichalcogenides and their unique physical and catalytic properties. *Scientific reports 6,* 34186 (2016).
59. Zhu, Zhiyong, Yingchun Cheng, and Udo Schwingenschlögl. Topological Phase Diagrams of Bulk and Monolayer TiS_{2-x} Te_x. *Physical review letters 110*, 7, 077202 (2013).